# Mars Entry, Descent, and Landing Instrumentation 2 Trajectory, Aerodynamics, and Atmosphere Reconstruction

Christopher D. Karlgaard*
*Analytical Mechanics Associates, Inc., Hampton, VA, 23666*

Mark Schoenenberger†, Soumyo Dutta†, and David W. Way†
*NASA Langley Research Center, Hampton, VA, 23681*

**On February 18th, 2021, the Mars 2020 entry system successfully delivered the Perseverance rover to the surface of Mars at Jezero Crater. The entry capsule carried a set of instrumentation installed on the heat shield and backshell, named the Mars Entry, Descent, and Landing Instrumentation 2. The instruments include pressure transducers, thermocouples, heat flux gauges, and radiometers to measure the aerodynamic and aerothermodynamic performance of the entry vehicle. This paper describes the trajectory and atmosphere reconstruction results based on the pressure sensor measurements. The process uses a Kalman filter approach to estimate the freestream atmospheric properties from the pressure measurements combined with a model of the pressure distribution of the heatshield and other sensor inputs, including an inertial measurement unit and other on-board navigation sensors, and several external atmospheric observations. The results indicate upper altitude density was up to 150% higher than nominal, which is consistent with the observed early entry guidance start time. The density below 40 km was within 12% the pre-flight predictions. The reconstructed axial force coefficient was approximately 2% lower than the pre-flight prediction across the flight range.**

## Nomenclature

| | | |
|---|---|---|
| $b$ | = | Aerodynamic reference length, m |
| $C_A, C_Y, C_N$ | = | Axial, side, and normal aerodynamic force coefficients |
| $g$ | = | Earth's standard gravitational acceleration, $g$ = 9.80665 m/s$^2$ |
| $I_{xx}, I_{yy}, I_{zz}$ | = | Vehicle moments of inertia in the spacecraft frame, kg-m$^2$ |
| $I_{xy}, I_{xz}, I_{yz}$ | = | Vehicle products of inertia (negative integrals) in the spacecraft frame, kg-m$^2$ |
| $m$ | = | Mass, kg |
| $\boldsymbol{P}_0$ | = | EMEJ2000 position and velocity covariance at $t_0$ |
| $R_e$ | = | Equatorial radius of Mars, m |
| $R_p$ | = | Polar radius of Mars, m |
| $\Re$ | = | Specific gas constant, J/kg-K |
| $\boldsymbol{r}_{imu}$ | = | Position of the IMU in the cruise frame, m |
| $T_{sc2ac}$ | = | Spacecraft frame to aerodynamic frame transformation matrix |
| $T_{imu2sc}$ | = | IMU instrument frame to spacecraft frame transformation matrix |
| $t$ | = | Time, s |
| $t_0$ | = | Initial time, s |
| $X_{cm}, Y_{cm}, Z_{cm}$ | = | Vehicle center of mass position in the cruise frame, m |
| $X, Y, Z$ | = | EMEJ2000 position components at $t_0$ |
| $\dot{X}, \dot{Y}, \dot{Z}$ | = | EMEJ2000 velocity components at $t_0$ |
| $\alpha$ | = | Angle of attack, deg |
| $\alpha_T$ | = | Total angle of attack, deg |
| $\beta$ | = | Angle of sideslip, deg |
| $\zeta_0, \zeta_1, \zeta_2, \zeta_3$ | = | Quaternion components of the EMEJ2000 to cruise frame attitude at $t_0$ ($\zeta_0$ is the scalar) |
| $\nu_0, \nu_1, \nu_2, \nu_3$ | = | Quaternion components of the EMEJ2000 to MCMF attitude at $t_0$ ($\nu_0$ is the scalar) |

*Supervising Engineer, Associate Fellow AIAA.
†Aerospace Engineer, Atmospheric Flight and Entry Systems Branch, Senior Member AIAA.

# I. Introduction

On February 18th, 2021, the Mars 2020 entry system [1] succesfully delivered the Perseverance rover to the surface of Mars at Jezero Crater. The entry capsule carried a unique set of instrumentation installed on the heat shield and backshell, named the Mars Entry, Descent, and Landing Instrumentation 2 (MEDLI2)[2, 3]. The instruments include pressure transducers, thermocouples, heat flux gauges, and radiometers to measure the aerodynamic and aerothermodynamic performance of the entry vehicle. The MEDLI2 sensor suite builds on the success of the Mars Entry, Descent, and Landing Instrumentation (MEDLI), which flew on the heatshield of the Mars Science Laboratory (MSL) Curiosity rover's entry capsule during its landing on Mars in August, 2012 [4–9]. The MEDLI2 sensor suite includes an enhanced set of instruments to make measurements in flight regimes and locations on the vehicle that were not captured in the MEDLI data. The layout of the sensors is shown in Figure 1. The sensor are divided into two main categories, the Mars Entry Atmospheric Data System (MEADS), measuring pressures, the Mars Integrated Sensor Plug (MISP) which are various types of aerothermal sensors that include thermocouples, heat flux gauges, and radiometers. Data from both sets of sensors was acquired by the Sensor Support Electronics (SSE) unit located on the heatshield structure. The individual sensor locations are labeled as MEADS Pressure on Heatshield (MPH), MEADS Pressure on Backshell, (MPB), MISP Thermal on Heatshield (MTH), and MISP Thermal on Backshell (MTB). The MEDLI2 sensors were powered on approximately 5 hours before atmospheric entry, and began storing data into a 20 minute buffer until being powered down approximately 10 seconds before heatshield separation.

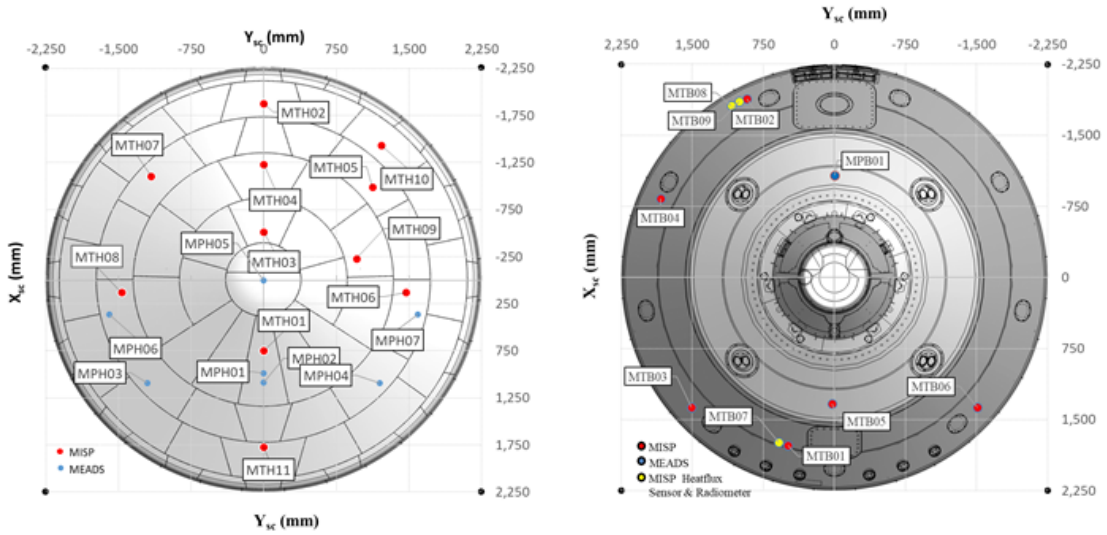


(a) Forebody

(b) Backshell

**Fig. 1 MEDLI2 Sensor Layout**

This paper describes the reconstruction of the entry capsule trajectory based on the MEADS pressure sensors. These sensors include seven pressure measurements on the heatshield at specific locations that are used to reconstruct the atmospheric-relative trajectory, and a single pressure measurement on the backshell to measure the base pressure acting on the vehicle in order to better understand the vehicle aerodynamic performance. There are three types of pressure transducers as part of the MEADS system. On the forebody there is one strain-gauge type transducer located in the predicted hypersonic stagnation point region (MPH1), with a full scale pressure range of 35 kPa. This transducer is a MEDLI flight spare, and is intended to measure the stagnation point pressure in the hypersonic flight regime. The remaining six heatshield pressures are measured by peizio-resistive type transducers with a full scale range of 7 kPa. These transducers are intended to provide improved resolution measurements in the supersonic flight regime. The supersonic regime transducers will be saturated during the hypersonic flight regime and will desaturate during entry prior to crossing the Mach 5 threshold. One pressure port is located at the predicted supersonic trim angle of attack stagnation point (MPH2), while another transducer is located at the vehicle nose to measure the zero trim stagnation pressure prior to parachute deployment (MPH5). The remaining four port locations were optimized as symmetric pairs (MPH3/MPH4 and MPH6/MPH7) distributed around the heatshield to produce minimum weighted covariance

trace measurements[10, 11], mainly providing observability of the angles of attack and sideslip. Finally, the backshell pressure is measured by a variable-reluctance type transducer with a full scale range of 700 Pa. The location of the pressure port (MPB1) was informed by free flight ballistic range tests[12].

The specific science requirements of the MEADS system are to provide data that can be used to reconstruct the atmospheric-relative trajectory, the as-flown atmosphere profile, and the as-flown aerodynamics of the capsule during atmospheric entry. The MEADS measurements are required to provide data with $3\sigma$ accuracies to enable the reconstruction of the vehicle axial force coefficient to within 2% and the atmospheric density to within 5% from just after atmospheric entry (when the freestream dynamic pressure is greater than 200 Pa) until deployment of the supersonic parachute. During the supersonic range of flight, defined as Mach 5 and below, the system is required to provide measurements enable the reconstruction of the aerodynamic flow angles to within 0.5 deg, the Mach number to within 0.1, and the atmospheric winds to within 10 m/s. Extensive pre-flight analysis, ground testing, and thermal calibrations were peformed to show that the sensors were able to produce measurements of sufficient accuracy to meet these science requirements. Due to scheduling, not all ground testing was completed on the flight units before they had to be instealled on the vehicle. Additional ground testing was performed after the Mars 2020 launch using flight spare sensors. This testing indicated some additional uncertainties due to transducer dynamic response that were not captured in the initial error budget, meaning that the angle of attack and wind reconstruction requirements would only be partially met [13].

Analysis of the MEDLI2 flight data also incorporates other measurement sources both from onboard and external sensors. Onboard sensors include navigation sensors such as the Descent Stage Inertial Measurement Unit (DIMU)[14] and the Terminal Descent Sensor (TDS)[15], both of which have flight heritage from the MSL landing in 2012. A new addition for the Perseverance landing in 2021 is the Lander Vision System (LVS)[16, 17], which provides Terrain Relative Navigation (TRN) position measurements based on camera images acquired during descent that are matched to a map of the planetary surface. These measurements are further aided by other external sources including Orbit Determination (OD) initial conditions [18], landing site position fixes based on High Resolution Imaging Science Experiment (HiRISE)[19, 20] imagery, atmospheric profiles from the Mars Climate Sounder (MCS)[21], and planetary surface atmospheric measurements from the Mars Environmental Dynamics Analyzer (MEDA)[22] instruments on board the Perseverance rover, reconstructed mass properties, and a model of the Mars gravity [23, 24]. A summary of the data sources used in the reconstruction is shown in Table 1.

**Table 1 Mars 2020 Reconstruction Data Sources**

| Source | Data Product |
|---|---|
| MEADS [3] | Heatshield and backshell pressures |
| DIMU [14] | 3-axis linear acceleration and angular rate |
| TDS [15] | Range and range rate |
| LVS [16, 17] | 3-axis relative position |
| OD [18] | Initial inertial position and velocity |
| Landing site [20] | Radius, declination, and longitude |
| MCS [21] | Temperature, pressure, and density vs. altitude |
| MEDA [22] | Surface pressure |
| Mass properties | Mass, inertia, center of mass |
| Gravity model [23, 24] | Gravitational acceleration |

These measurement sources are combined using a Kalman filter method to produce a best estimate of the capsule entry trajectory. The reconstruction method makes use of the New Statistical Trajectory Estimation Program (NewSTEP)[25–28] Kalman filtering code to reconstruct the trajectory from the available data. The approach uses a sequence of two Iterative Extended Kalman-Schmidt Filter-Smoothers to estimate the trajectory. The first filter is a purely kinematic filter in which the DIMU data is combined with the TDS, LVS, OD initial conditions, and landing site location to produce an estimate of the inertial and planet-relative trajectory. Next, this reconstructed trajectory is an input to a dynamic filter in which the MEADS measurement data are processed with a simplified atmospheric dynamics model based on the

hydrostatic equation and ideal gas law to produce estimates of the atmospheric-relative state and atmospheric conditions along the trajectory[11]. The atmospheric-relative state (dynamic pressure) is then used with vehicle mass properties to compute estimates of the as-flown aerodynamics.

The remainder of this paper is organized as follows. Section II describes several coordinate frames that are used for the reconstruction of the Mars 2020 EDL trajectory. Section III discusses the data sources that are used for the reconstruction. The results of the reconstruction are described in Section IV. Results of the aerothermal reconstruction based on the MISP sensors can be found in [29–32].

## II. Coordinate Frames

The Earth Mean Equator and Equinox of Epoch January 2000 (EMEJ2000) [33] inertial reference system is defined by the Z axis normal to the Earth mean equator at the epoch of J2000 (Julian date of 2451545.0) and the X axis parallel to the vernal equinox of the Earth mean orbit at J2000. The Mars-Centered Mars-Fixed (MCMF) frame is defined by the Z axis normal to the equator of Mars and the X axis aligned through the prime meridian. In each frame, the Y axis is chosen to complete the right-handed system.

The Areocentric (AC) frame has its origin at the vehicle center of mass, with the Z axis oriented toward the center of the planet, the X axis normal to the radius vector in the northerly direction, and Y axis is to the East. The Areodetic (AD) frame is defined similarly to the AC frame but has its Z axis perpendicular to the reference ellipse (defined by $R_e$ = 3396190 m and $R_p$ = 3376200 m [34]) and X axis tangent to the reference ellipse in the north direction. The Y axis of the AD frame is the same as that of the AC frame. The Areodetic frame is also commonly referred to as the North-East-Down (NED) frame.

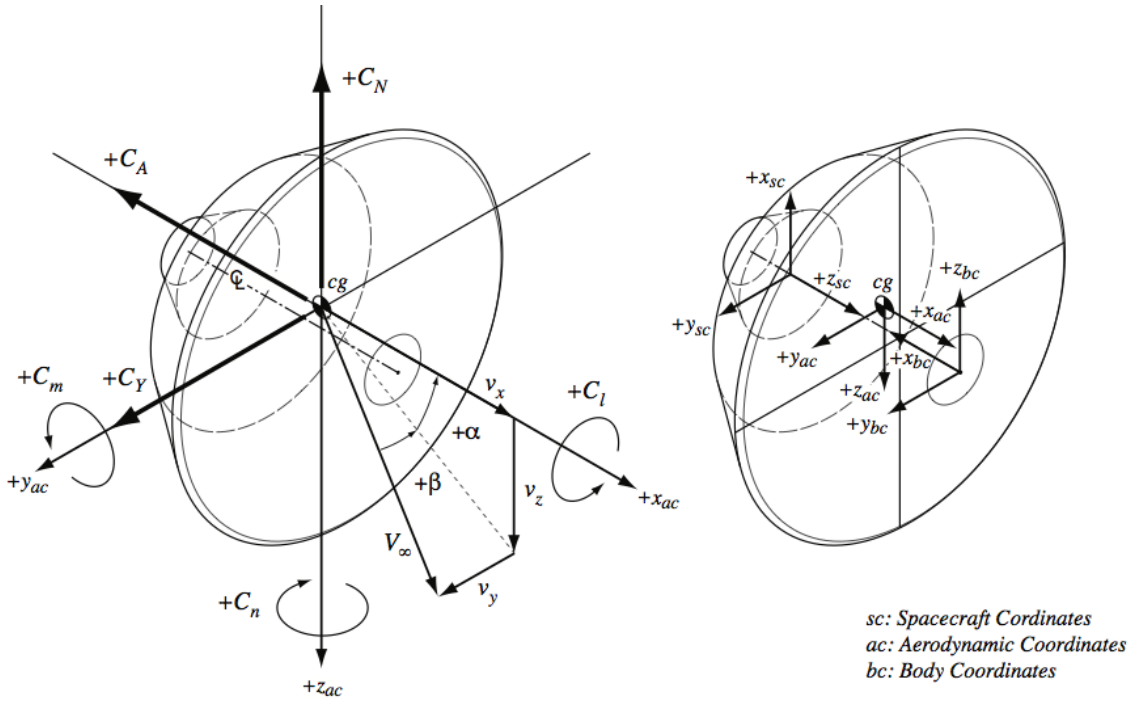


**Fig. 2 Vehicle Coordinate Frames**

Vehicle coordinate frames relevant to the aerodynamics and flight mechanics are shown in Figure 2. The axes labeled $x_{sc}$, $y_{sc}$, and $z_{sc}$ are the axes of the spacecraft coordinate frame and the axes labeled $x_{ac}$, $y_{ac}$, and $z_{ac}$ define the aerodynamic coordinate frame. Directions of the aerodynamic force coefficients $C_A$, $C_Y$, and $C_N$ are shown as are the definitions of the aerodynamic flow angles. The transformation from the spacecraft frame to the aerodynamics

frame is given by

$$T_{sc2ac} = \begin{bmatrix} 0 & 0 & 1 \\ 0 & 1 & 0 \\ -1 & 0 & 0 \end{bmatrix} \tag{1}$$

The DIMU instrument frame [35] is defined by the axes internal to the IMU in which the three-axis accelerations and angular rates are measured. The location of the DIMU in the spacecraft reference frame is given by the vector $\boldsymbol{r}_{imu} = [\ 0.8684815 \quad -0.6407693 \quad 0.6077792\ ]^T$ m. The transformation from the IMU instrument frame to the spacecraft reference frame is given by the matrix

$$T_{imu2sc} = \begin{bmatrix} -0.872975115990299 & 0.343162856206043 & 0.346631938779788 \\ -0.487764416945555 & -0.614998742299899 & -0.619566316491871 \\ 0.000566059614137526 & -0.709940702516804 & 0.704261228867854 \end{bmatrix} \tag{2}$$

## III. Data Sources

### A. Mars Entry Atmospheric Data System

The MEADS pressure measurements aqcuired during the Mars 2020 EDL are shown in Figure 3. Note that the time $t = 0$ corresponds to the on-board navigation initialization time. The measurements were sampled by the SSE at a rate of 2048 Hz. The measurements were stored into a buffer of 256 samples that were averaged and then stored in memory at a rate of 8 Hz. The measurements were stored on-board the rover and then sent back to Earth after landing, although a subset of the measurements were transmitted in real-time during EDL. After recepit of the data on Earth, the measurement data were converted from raw counts into sensor milli-Volt outputs. Thermal calibrations were performed based on the milli-Volt outputs and the measured sensor temperatures to convert the data into units of pressure [13]. An in-flight zero was performed prior to atmospheric entry in order to remove any residual offsets. The magnitude of the zero offsets were similar to those observed during two cruise checkouts conducted in October and November 2020. There were no data dropouts. Some spikes in the data were observed at the times of pyro/shock events such as Entry Ballast Mass (EBM) jettison and parachute mortar fire. These spikes were removed from the data. A time shift of 60.625 ms was applied to the data to account for the lag induced by the on-board averaging filter [13].

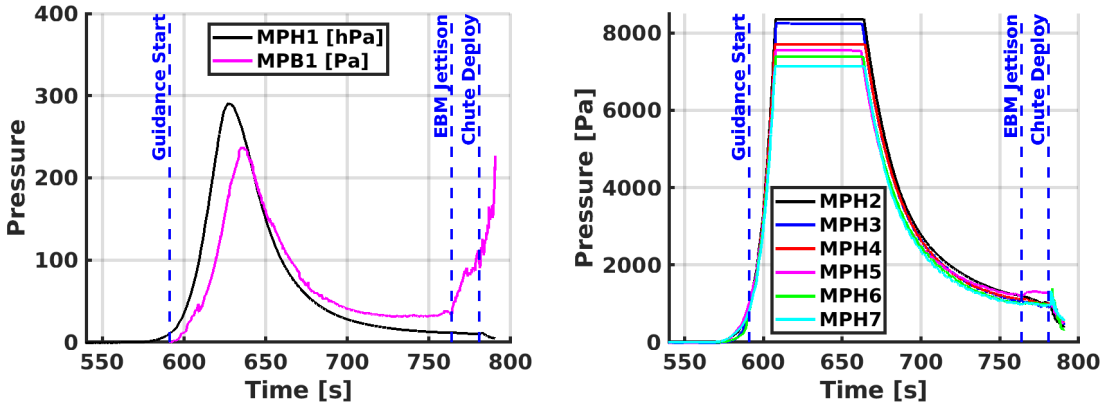


(a) Hypersonic and Backshell (b) Supersonic

**Fig. 3 Mars Entry Atmospheric Data System Pressure Measurements**

The hypersonic range stagnation pressure transducer MPH1 recorded a peak pressure of 29.07 kPa at a reconstructed Mach number of 17.24 at an altitude of 21.74 km. The supersonic range transducers recorded data at high altitude prior to saturating, then desaturated prior to reaching supersonic flight conditions. Each supersonic transducer has its output clipped at 42.8 mV, but since each unit has slightly different sensitivities, the corresponding staturation pressure is different from unit to unit. Specifically, transducers MPH2 through MPH7 saturated at 8.37, 8.25, 7.71, 7.55, 7.40, and

7.15 kPa, respectively. MPH4 was the first transducer to saturate after entry, and was the last transducer to desaturate as the vehicle approached the supersonic flight regime. MPH4 saturation occured at a reconstructed Mach number of 24.45 and altitude of 40.01 km. MPH4 desaturation occured at a reconstructed Mach number of 6.32 and an altitude of 14.07 km. Each transducer met the requirement to report data at pressure levels of 7 kPa and below during the supersonic flight regime. The peak recorded pressure on the backshell from sensor MPB1 was 242 Pa, at a reconstructed Mach number and altitude of 13.78 and 18.28 km, respectively.

### B. Descent Stage Inertial Measurement Unit

An important measurement source for performing the trajectory and atmosphere reconstruction is the on-board Descent Stage Inertial Measurement Unit (DIMU), a Honeywell Miniature Inertial Measurement Unit (MIMU), consisting of QA3000 accelerometers and GG1320 ring laser gyroscopes [35]. The DIMU provides three-axis linear acceleration and angular rate measurements in the DIMU instrument frame at a sample rate of 200 Hz. The measured accelerations were transformed from the DIMU frame into the vehicle body frame (using the reconstructed mass properties described in Section III.G for the center of mass location) using the transformation matrices given in Equation 1 and 2 for integration in order to propagate the states from the initial condition. The data includes a scale factor correction of -9.80109e-07 to the body x-axis gyroscope, which was determined during the cruise phase to Mars.

Note that the numerical integration of these data for propagating the vehicle state makes use of the raw accelerations with no filtering. A second-order Butterworth filter [36] with a 5 Hz cutoff frequency (chosen to encapsulate the expected range of the capsule rigid body dynamics) is also applied to smooth the data for use in the aerodynamic reconstruction. The filter is applied in forward/backward mode to eliminate phase loss [37]. The raw and filtered accelerations and angular rates are shown in Figure 4.

The DIMU was modeled using the error parameters specified in Table 2 provided in [38]. The error parameters include bias, scale factor, misalignment, noise, and quantization. These uncertainties were modeled as consider parameters [33] in the Kalman filter so that the reconstructed state uncertainties are more realistic based on the accelerometer and gyroscope measurement uncertainties.

**Table 2 DIMU Error Parameters**

| Error Parameter | Accelerometer | Gyroscope |
|---|---|---|
| Misalignment ($3\sigma$) | 0.05 deg | 0.05 deg |
| Noise ($3\sigma$) | 150 $\mu$g | 0.0042 deg/s |
| Scale Factor ($3\sigma$) | 525 ppm | 15 ppm |
| Bias ($3\sigma$) | 300 $\mu$g | 0.15 deg/hour |
| Quantization | 0.54 m/s$^2$ | 0.0115 deg/s |

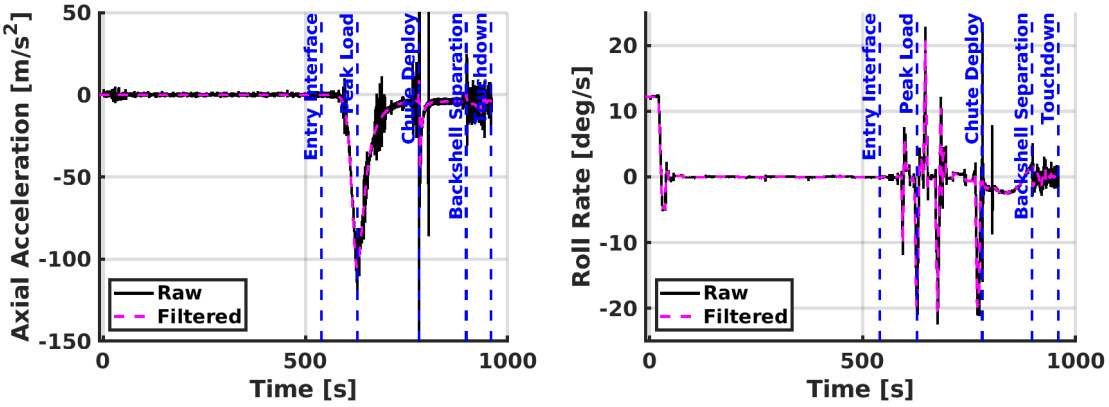


(a) Axial Acceleration




(b) Roll Rate

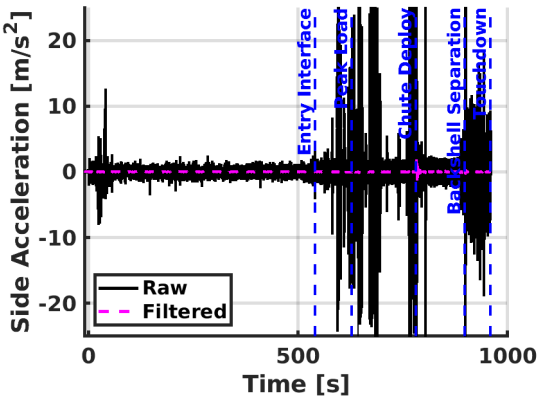


(c) Side Acceleration

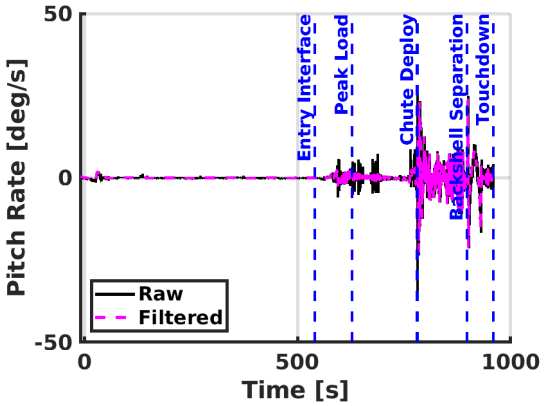


(d) Pitch Rate

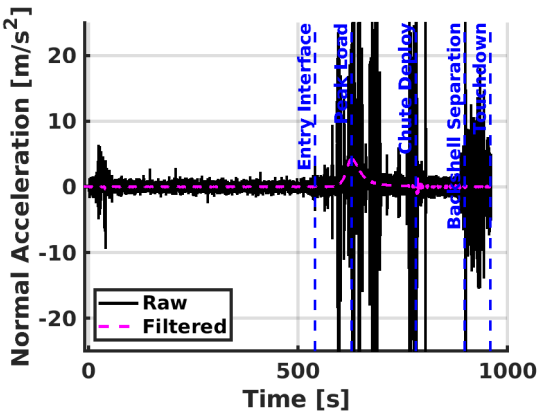


(e) Normal Acceleration

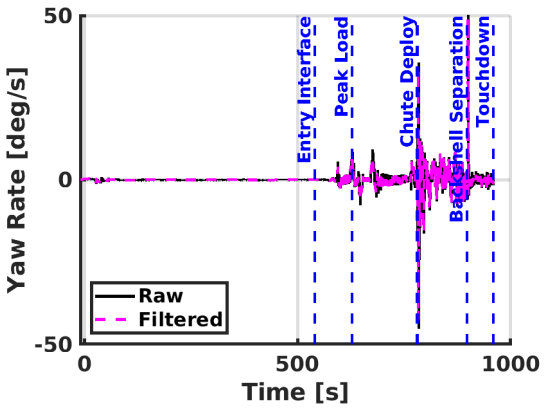


(f) Yaw Rate

**Fig. 4 Accelerations and Angular Rates in Aerodynamic Coordinate Frame**

### C. Terminal Descent Sensor

After heatshield separation, the Terminal Descent Sensor (TDS) was activated to make range and range-rate measurements from the sensor to the ground. The TDS consists of six Ku-band radar beams that provide measurements at a rate of 20 Hz from alternating beams [14, 35]. These measurements were used in the trajectory reconstruction process to provide position and velocity data in the form of range and range-rate that can be processed by the Kalman

filter to improve the trajectory estimate. The range and range-rate data are shown in Figure 5. The measurement uncertainties are shown in Table 3. The misalignments, bias, and scale factor uncertainties were modeled as consider parameters in the filter.

**Table 3 TDS Error Parameters**

| Error Parameter | Range | Range Rate |
|---|---|---|
| Sensor Misalignment ($3\sigma$) | 0.28 deg | 0.28 deg |
| Beam Misalignment ($3\sigma$) | 0.207 deg | 0.207 deg |
| Noise ($3\sigma$) | 0.15 m | 0.015 m/s |
| Scale Factor ($3\sigma$) | 0.009 | 0.0015 |
| Bias ($3\sigma$) | 0.3 m | 0.03 m/s |
| Quantization | 1 mm | 0.5 mm/s |

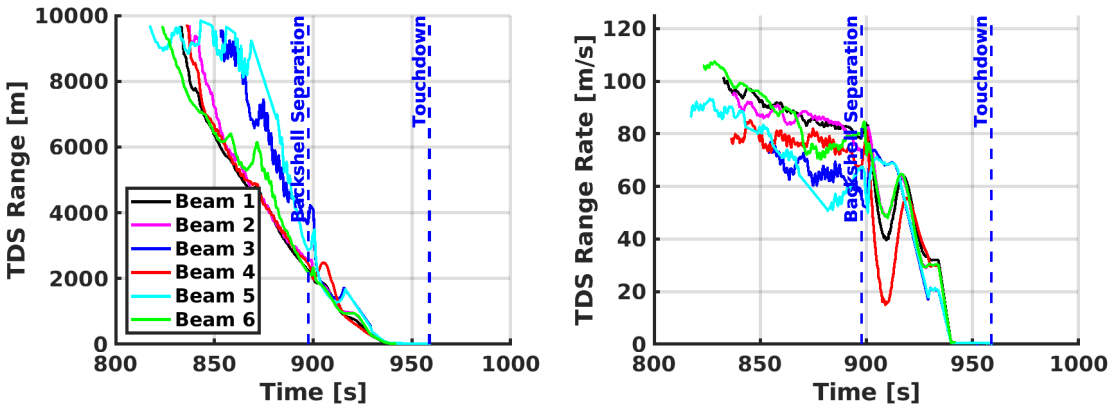


(a) Range (b) Range Rate

**Fig. 5 Terminal Descent Sensor Data**

Processing of this data in the Kalman filter requires a terrain model of the surface of the planet. The model used in the filter is based on a Digital Elevation Map (DEM) [39] of the landing site region with 1 m resolution.

### D. Terrain Relative Navigation

The Terrain Relative Navigation (TRN) system was a new addition to the Mars 2020 EDL GN&C that did not exist at the time of MSL. The TRN system acquires images of the surface of the planet during descent and uses an on-board database to determine the three-axis position of the vehicle relative to the image database [16], which can be used as another position fix in the Kalman filter. The TRN system acquired 42 such position fixes during the vehicle descent to the surface. The TRN altitude channel is shown in Figure 6 as an example of one-axis, but all three axes were processed by the filter as a position update. The measurements were assumed to have a $3\sigma$ uncertainty of 40 m in each axis, based on the TRN system requirements specification [16]. Post-flight analysis of the TRN performance indicates the actual accuracy is likely to have been far better than the requirement [17].

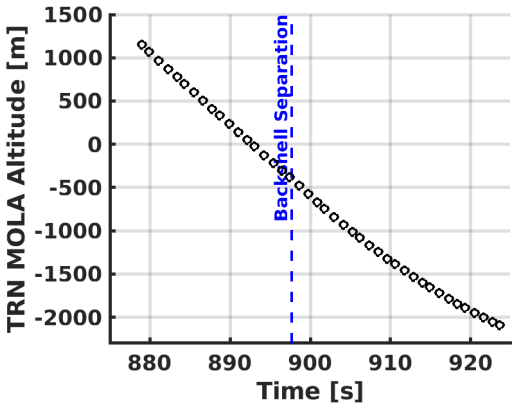


**Fig. 6 TRN MOLA Altitude Estimate**

### E. Initial Conditions

The initial conditions used for the reconstruction are based on the orbit determination (OD) solution OD138 [18]. The states are provided in the EMEJ2000 inertial frame at a spacecraft clock time (SCLK) of 666951969.6604 s. The position and velocity components are listed in Table 4. The covariance of the EMEJ2000 initial states is given in Equation 3.

**Table 4 EMEJ2000 Orbit Determination 138 Initial Conditions**

| Coordinate | Initial Condition |
|---|---|
| $t$, s | 666951969.6604 |
| $X$, m | 630770.944374511 |
| $Y$, m | -4780173.77671539 |
| $Z$, m | -469876.729166781 |
| $\dot{X}$, m/s | 3217.26453803849 |
| $\dot{Y}$, m/s | 3575.35545638128 |
| $\dot{Z}$, m/s | -1030.24301362414 |

$$\boldsymbol{P}_0 = \begin{bmatrix} 5.5555 & 8.5848 & 8.1124 & 5.1272\text{e}{-3} & -1.1336\text{e}{-3} & -5.6597\text{e}{-4} \\ 8.5848 & 1.6135\text{e}1 & 1.4500\text{e}1 & 7.1559\text{e}{-3} & -1.3370\text{e}{-3} & -1.2298\text{e}{-3} \\ 8.1124 & 1.4500\text{e}1 & 1.4798\text{e}1 & 6.9149\text{e}{-3} & -2.0265\text{e}{-3} & -4.4950\text{e}{-4} \\ 5.1272\text{e}{-3} & 7.1559\text{e}{-3} & 6.9149\text{e}{-3} & 1.1658\text{e}{-5} & -7.4043\text{e}{-7} & -5.9725\text{e}{-7} \\ -1.1336\text{e}{-3} & -1.3370\text{e}{-3} & -2.0265\text{e}{-3} & -7.4043\text{e}{-7} & 8.6287\text{e}{-6} & 2.3773\text{e}{-7} \\ -5.6597\text{e}{-4} & -1.2298\text{e}{-3} & -4.4950\text{e}{-4} & -5.9725\text{e}{-7} & 2.3773\text{e}{-7} & 8.1365\text{e}{-6} \end{bmatrix} \quad (3)$$

The attitude initial conditions were extracted from the onboard navigation state at the $t_0$ time, and then propagated back in time using the gyroscope measurements to align with the OD138 initial position and velocity. The closest DIMU measurement time to the OD138 time is 666951969.660815 s. The attitude conditions at this time are listed in Table 5. The $3\sigma$ uncertainties are assumed to be 0.1 deg in each axis, uncorrelated, which was the best estimate of the attitude initialization uncertainty prior to EDL. Post-flight analysis has indicated the actual uncertainty was slightly better than anticipated at a $3\sigma$ value of 0.08 deg [40]. The OD138 conditions were propagated ahead for reconstruction initialization to match with the closest DIMU sample time so that the position, velocity, and attitude conditions are provided at the same instant in time.

**Table 5 EMEJ2000 Spacecraft Frame Attitude Initial Conditions**

| Quaternion | Initial Condition |
|---|---|
| $t$, s | 666951969.660815 |
| $\zeta_0$ | 0.750565992359049 |
| $\zeta_1$ | -0.297847161876377 |
| $\zeta_2$ | 0.532251853308867 |
| $\zeta_3$ | 0.254255233821332 |

The orientation of Mars with respect to the EMEJ2000 frame is also required in order to compute the planet-relative trajectory. The MCMF frame is defined relative to the EMEJ2000 frame at $t_0$ by the quaternion listed in Table 6. The MCMF frame alignment was propagated to other epochs as required, using a planetary angular rate of 7.088 218 066 303 86e−5 deg/s normal to the equator.

**Table 6 EMEJ2000 MCMF Frame Initial Conditions**

| Quaternion | Initial Condition |
|---|---|
| $t$, s | 666951979.500504 |
| $\nu_0$ | 0.49902685255 |
| $\nu_1$ | -0.087190880612 |
| $\nu_2$ | 0.30617747138 |
| $\nu_3$ | -0.80599336647 |

### F. Landing Site Location

The Mars 2020 landing site location is shown in Table 7. This landing site corresponds to a Mars Orbiter Laser Altimeter (MOLA) [41] elevation of -2569.91 m. This location is used for trajectory reconstruction purposes to provide an end point to the trajectory as another form of a position fix, and was used to initialize the position state for the backward filtering pass. The landing site was determined by matching features from lander images with those captured from High Resolution Imaging Science Experiment (HiRISE) [19] onboard the Mars Reconnaissance Orbiter (MRO).

**Table 7 Landing Site Coordinates**

| Coordinate | Value | $3\sigma$ |
|---|---|---|
| Radius | 3391936.53 m | 5 m |
| Longitude | 77.45088572 deg | 8.4353e-4 deg |
| Declination | 18.44462715 deg | 8.4353e-4 deg |

### G. Mass Properties Reconstruction

The vehicle mass properties were reconstructed based on the as-flown timeline and commanded thruster firing history. The analysis is based solely on the cumulative fuel use estimated by the on-board GN&C logic, and not by any real-time sensor measurements. These on-board estimates assumed a conservative specific impulse and likely

overestimated the actual fuel use. The goal of the mass property reconstruction is to convert the estimated fuel use into a time-accurate estimate of the mass and center of gravity of the composite wet vehicle throughout EDL. The telemetry provides only the total cumulative fuel use and does not account for Mars Lander Engines (MLE) priming. The reconstructed propellant mass time history accounts for the MLE priming and propellant use drawn from each tank according to the nominal depletion ratio and the RCS command history. Total vehicle wet mass properties were then computed based on the reconstructed propellant masses and the vehicle dry component mass properties.

### H. Gravity Model

The Mars gravitational acceleration is modeled using the MRO110C model [23]. This model is based on tracking data of Mars Global Surveyor (MGS), Mars Odyssey, MRO, and MOLA-derived topography data. The model contains spherical harmonics up to degree and order 110. A high fidelity localized gravity vector was generated for use close to the landing site [24]. This gravity model was used for radius values below 3420.0 km. The model consists of two gravity vectors, one a radius of 3420.0 km and one for the radius of the landing surface (3391.953 km), and in between these radius values the effective gravity was computed by a linear interpolation based on the radius.

## IV. Reconstruction Results

The Mars 2020 as-flown trajectory, atmosphere, and aerodynamics were reconstructed based on the data sources described in the previous section. The reconstruction was performed using separate Kalman filters. The first was a kinematic filter to reconstruct the inertial trajectory of the vehicle during EDL, and the second was a dynamic filter to reconstruct the atmosphere along the reconstructed inertial trajectory. This section describes the results of the reconstruction.

### A. Filter Residuals

The reconstructed trajectory was fit through all the available measurement data. Some examples of the filter residuals are shown in Figure 7. The residuals indicate good filter performance and that the data in general lacked any major anaomlaies or outliers. Systematic error in the pressure transducers were removed by iteratively fitting a second-order response model in order to minimize the mean square residual error. The initial guess for the coefficients of the model was based on dynamic calibration tests of the flight spare units that was conducted after the Mars 2020 launch. The response model was the tuned by the filter in order to construct individual response models for each flight transducer in order to minimize systematic error. An example of the results are shown in Figure 7(d), which shows the first pass and the final converged residuals for the MPH1 hypersonic pressure transducer. Note the reduction of systematic error between the first and final iteration. The residuals are essentially zero during the period where the supersonic transducers are saturated and thus not included in the reconstruction. The filter only has the single pressure measurement to process and so the solution converges directly onto the measured value. While the supersonic transducers are reading valid pressures the filter is determining a best fit to all seven measurements.

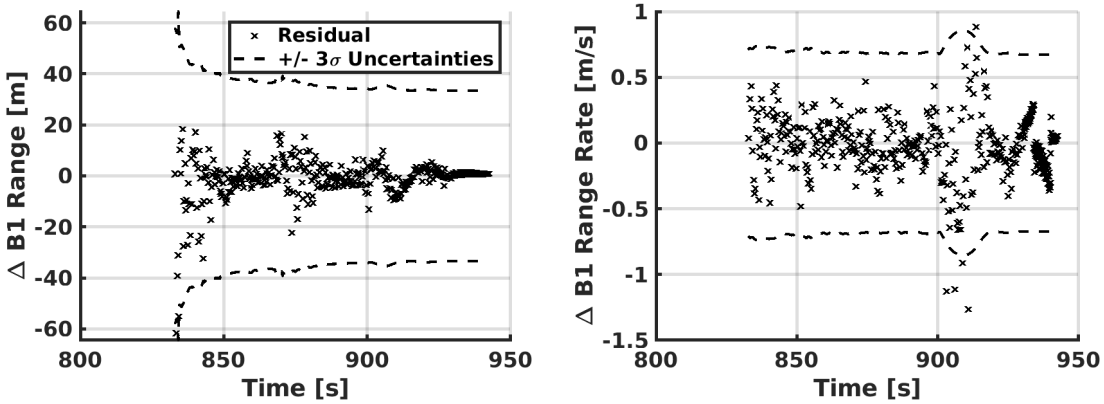


(a) TDS Beam 1 Range Residual

(b) TDS Beam 1 Range Rate Residual

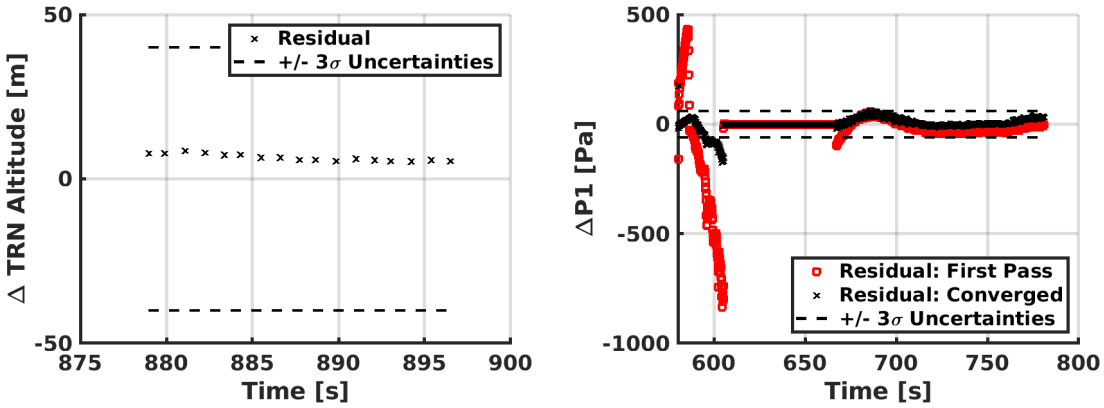


(c) TRN Altitude Residual

(d) Hypersonic Pressure Residual

**Fig. 7 Filter Residuals**

### B. Inertial Trajectory

Components of the vehicle trajectory relative to the Mars surface are shown in Figure 8 along with the OD138 initial conditions and the landing site location. Events along the trajectory are also indicated. Position and velocity uncertainties are shown in Figure 9. The entry interface altitude was calculated as the point in time where the vehicle crosses a radius value of 3522.2 km. The corresponding MOLA altitude at entry interface is 128.22 km. The planet-relative velocity magnitude and flight path angle are shown in Figure 10. The reconstructed velocity magnitude at entry interface is 5333.6 m/s. The reconstructed relative flight path angle at entry interface is -16.18 deg and the corresponding heading angle is 100.28 deg. The reconstructed velocity magnitude at touchdown is 0.828 m/s. The vehicle body Euler angles relative to the North-East-Down frame along with the total attitude uncertainty are shown in Figure 11. The total attitude uncertainty is shown in Figure 11(d). Further details of the vehicle trajectory performance compared to pre-flight predictions can be found in [42].

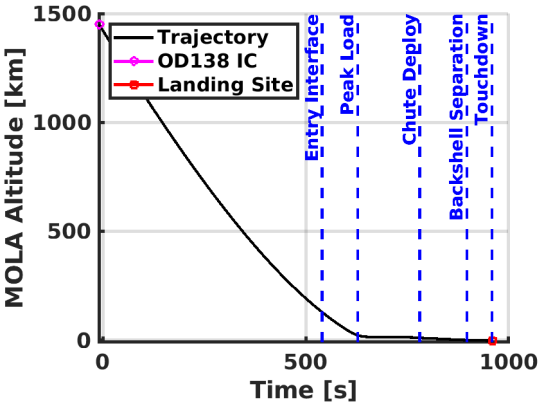


(a) MOLA Altitude

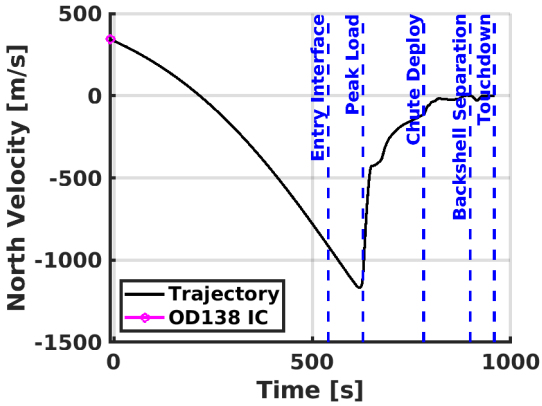


(b) North Velocity

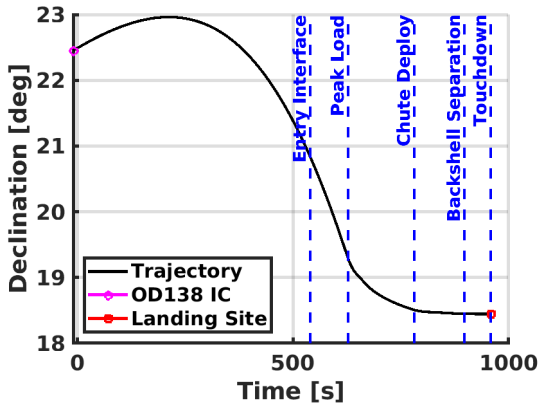


(c) Declination

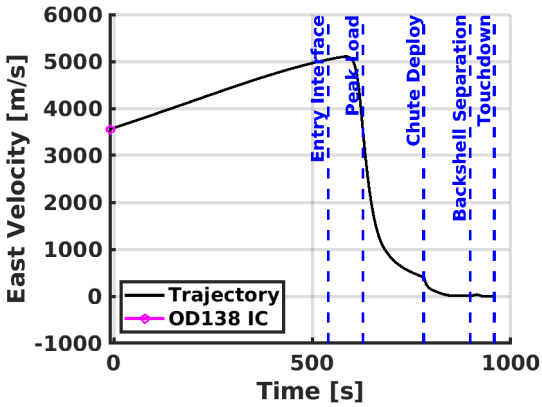


(d) East Velocity

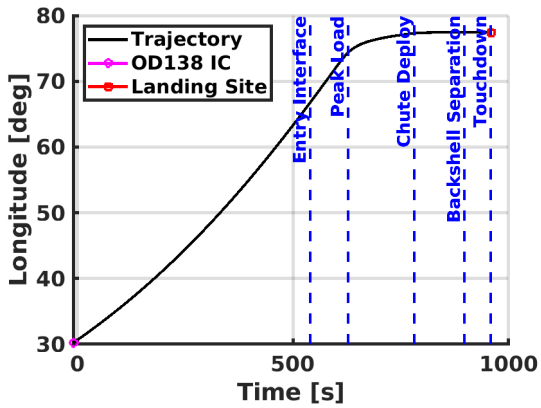


(e) Longitude

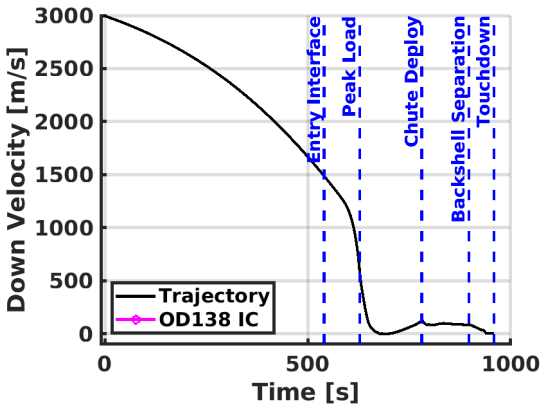


(f) Down Velocity

**Fig. 8 Reconstructed Position and Velocity**

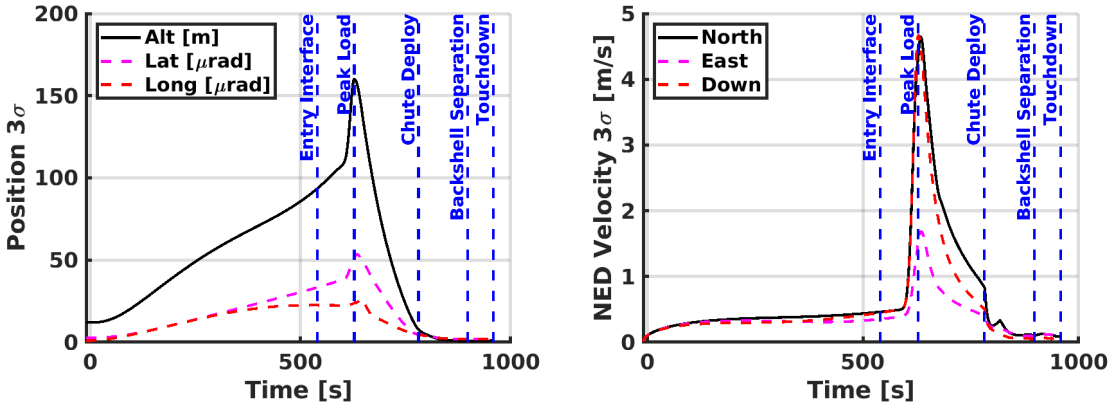


(a) Position (b) Velocity

**Fig. 9 Reconstructed Position and Velocity Uncertainties**

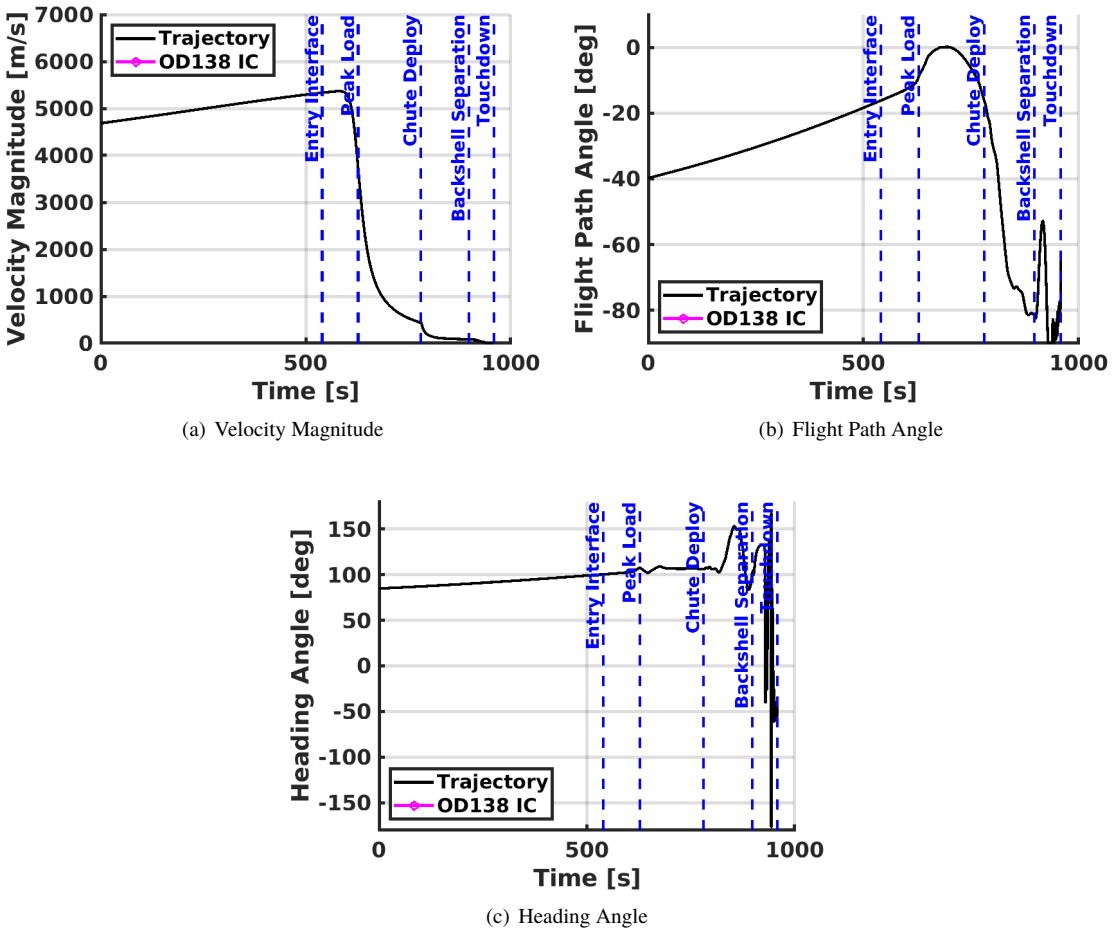


(a) Velocity Magnitude (b) Flight Path Angle

(c) Heading Angle

**Fig. 10 Reconstructed Velocity, Flight Path Angle, and Heading Angle**

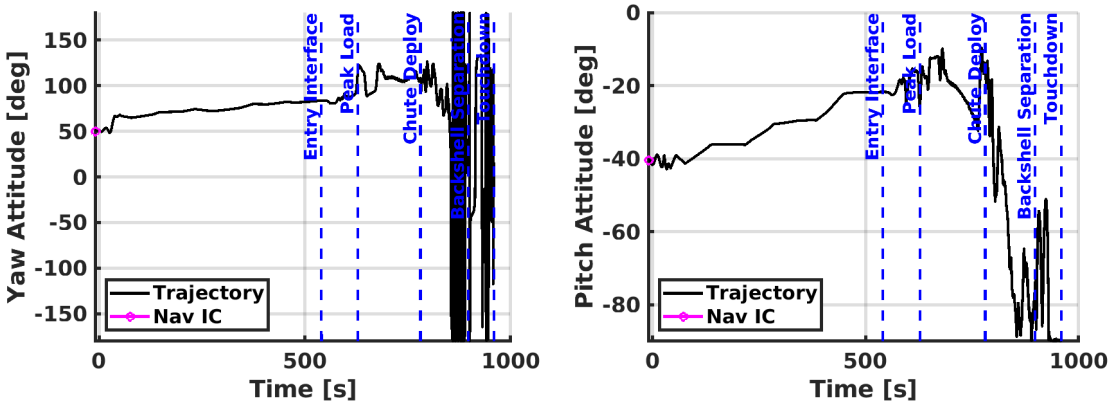


(a) Yaw




(b) Pitch

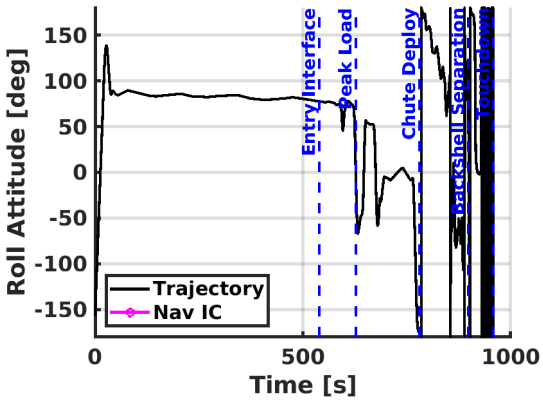


(c) Roll

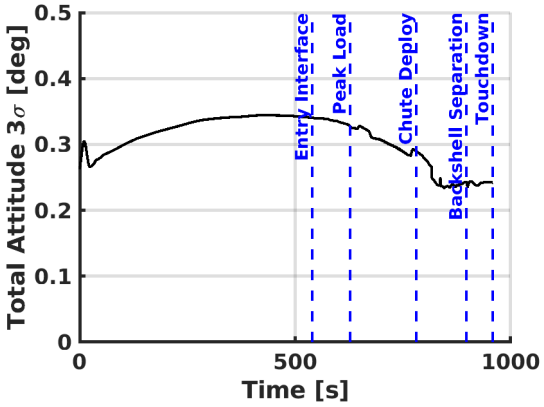


(d) Uncertainty

**Fig. 11 Reconstructed Attitude**

### C. Atmospheric-Relative Trajectory

This section describes the results of the MEADS reconstruction, based on the reconstructed inertial trajectory and the forebody pressure measurements. As described previously, the MEADS reconstruction process involved an iterative approach in which the pressure measurements were corrected by a second-order response model where the coefficients were computed to minimize the mean square error between the measured pressure and the CFD pressure model. The results of the MEADS reconstruction are compared to the results from a reconstruction based on the classical approach making of the nominal aerodynamics and measured accelerations to solve for the atmospheric-relative trajectory [43].

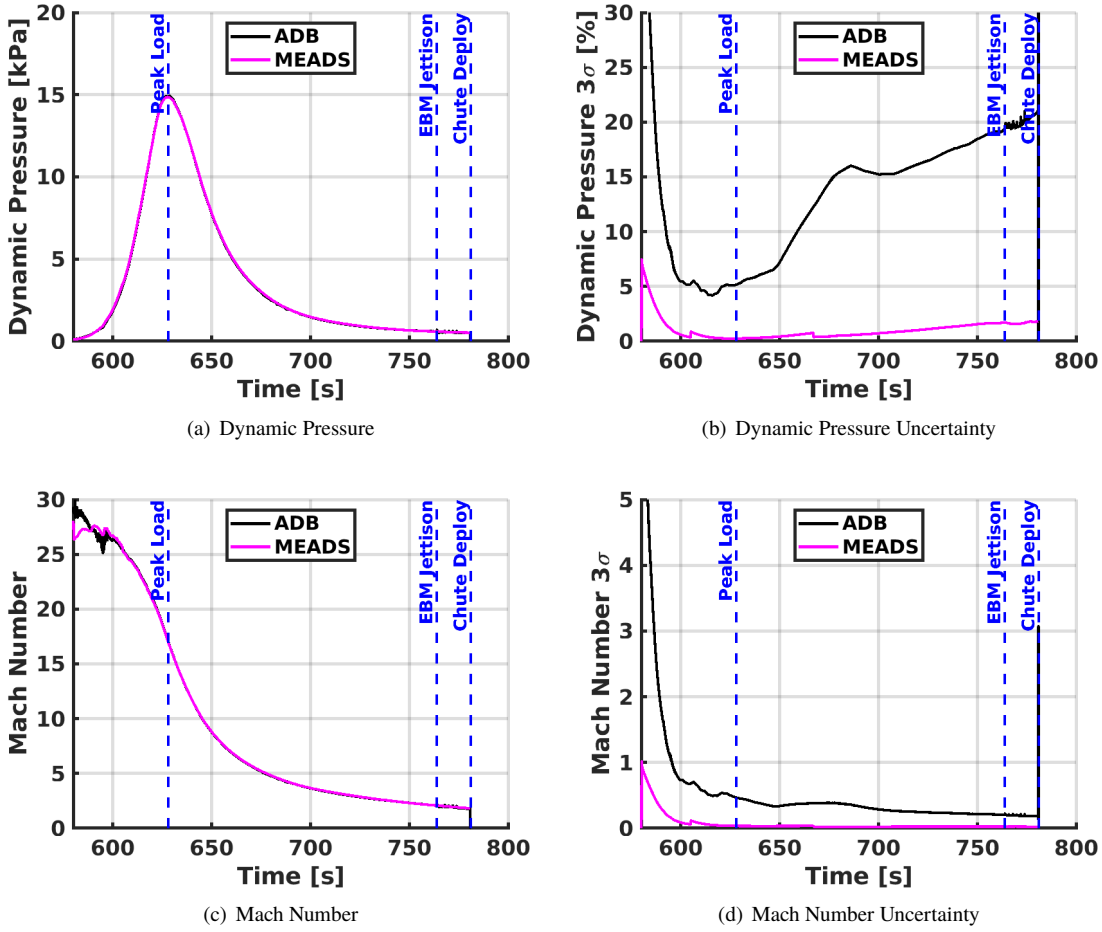


(a) Dynamic Pressure

(b) Dynamic Pressure Uncertainty

(c) Mach Number

(d) Mach Number Uncertainty

**Fig. 12 Reconstructed Dynamic Pressure and Mach Number**

The reconstructed Mach number and dynamic pressure are shown in Figure 12, with the classical aerodatabase reconstruction results indicated as ADB. The two reconstructions are in fairly good agreement. The peak dynamic pressure from the MEADS reconstruction is 14.87 kPa whereas the value from the aerodatabase reconstruction is approximately 0.5% higher at 14.94 kPa. The dynamic pressures from the MEADS and ADB reconstructions at parachute mortar fire are 522.8 and 464.4 Pa, respectively. The Mach number at high altitudes from the aerodatabase method exhibits some transient behavior, which is not unexpected as the uncertainties in that flight regime are high. Otherwise the two reconstructed Mach number time histories are in agreement. The MEADS and ADB reconstructed Mach number at parachute mortar fire are 1.82 and 1.75, respectively. Note that the ADB reconstructed uncertainties are larger than those of the MEADS reconstruction over the entire trajectory, especially in the supersonic flight regime where all MEADS pressures are recording data and the aerodatabase itself has the highest uncertainty.

The aerodynamic flow angles and their associated uncertainties are shown in Figure 13. Note that during the hypersonic flight phase the only active MEADS port is the stagnation point measurement, and the measurement sensitivity to flow angles is small. In effect, the flow angles derived from the MEADS measurements in the hypersonic

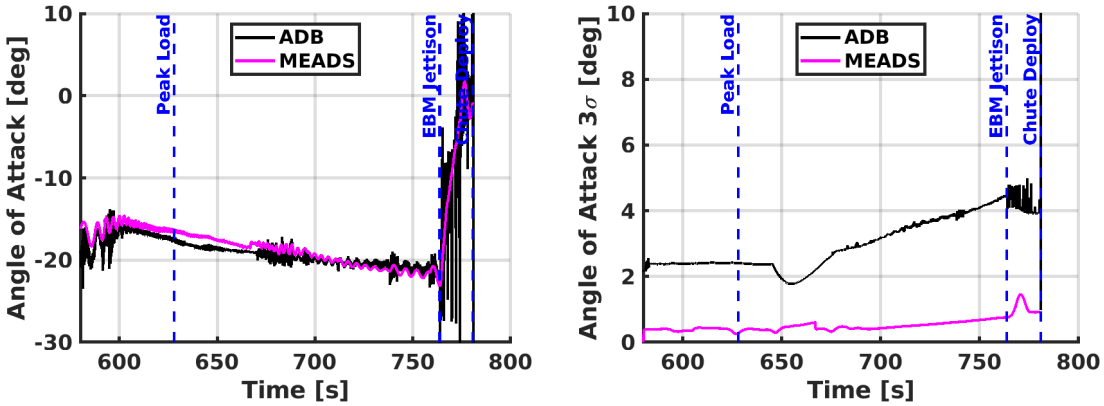


(a) Angle of Attack




(b) Angle of Attack Uncertainty

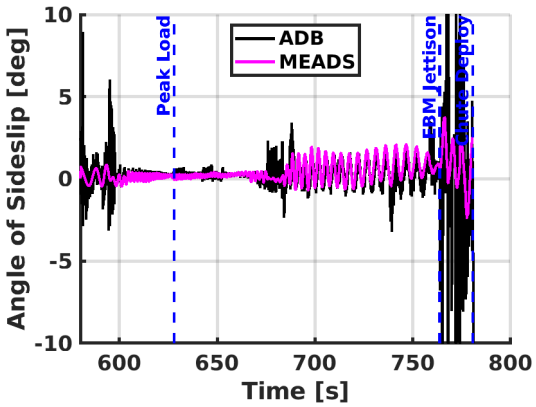


(c) Angle of Sideslip

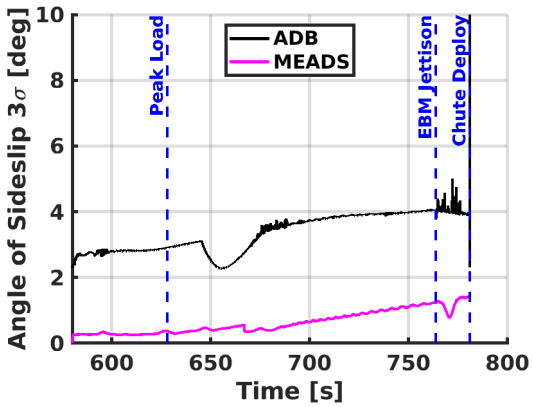


(d) Angle of Sideslip Uncertainty

**Fig. 13 Reconstructed Aerodynamic Flow Angles**

flight phase are almost identical to the angles derived from the planet-relative attitude reconstruction and assumed initial wind profile. All pressure ports are active during the supersonic flight range and thus the filter is able to estimate flow angles by fitting all the available measurements. The ADB reconstructed flow angles exhibit more noise than the MEADS reconstruction, which is also reflected in that the ADB flow angle uncertainties are large compared to the MEADS reconstruction. The two reconstructions are generally in agreement with differences of approximately 0.5 deg noticable in the hypersonic flight phase. Similar differences were noted in the MSL reconstruction [5].

### D. Aerodynamics

The vehicle aerodynamics were reconstructed based on the reconstructed atmospheric-relative trajectory, reconstructed mass properties, and measured angular rates and linear accelerations (after translation to the vehicle center of mass). The nominal aerodynamic database was also queried along the reconstructed atmospheric-relative trajectory. The axial force coefficient is shown in Figure 14(a). The reconstructed axial force coefficient is consistently below the nominal aerodatabase value, ranging from 0.5% to 2% different. This result is notably different than the MEDLI result for MSL, which indicated an axial force coefficient roughly 1% higher than the nominal value [6]. In either case, the reconstructed values are within the uncertainties of the aerodatabase.

Static stability derivatives were estimated by fitting a phase-shifted sinusoid through the measured angular rates during quiescent periods of flight where there were no RCS thruster firings. The static stability derivatives were computed from the resulting sinusoid frequency term, mass properties, and the reconstructed dynamic pressure [44]. The resuts are shown in Figure 14(b), along with the nominal stability deriatives computed along the reconstructed

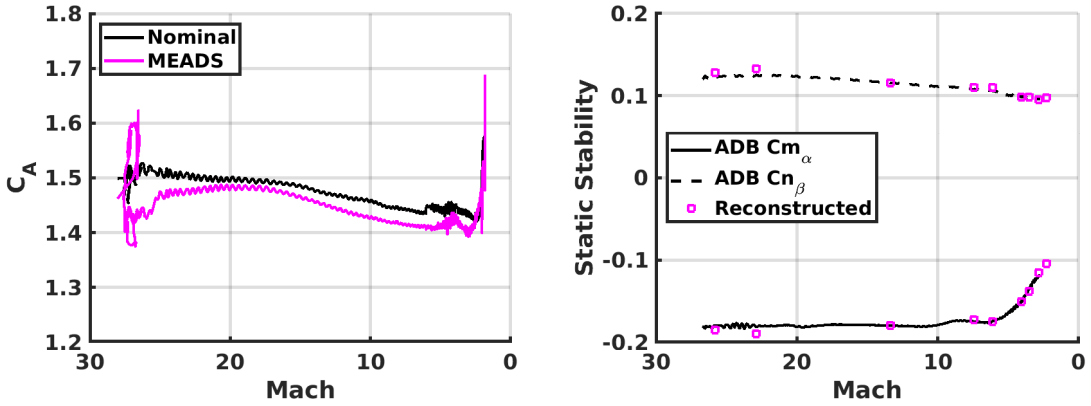


(a) Axial Force Coefficient

(b) Static Stability Derivatives

**Fig. 14 Reconstructed Aerodynamics**

trajectory. The results are similar to those from MSL, showing a good agreement between the reconstructed values and the nominal aerodynamics [6]. Further details on the reconstructed aerodynamic performance of the Mars 2020 entry capsule including analysis of the backshell MEADS pressure measurement can be found in [45].

### E. Atmosphere

Atmospheric condition along the trajectory were reconstructed directly from the MEADS pressure measurements and the reconstructed inertial trajectory. Density and pressure were estimated as states in the filter, and temperature was computed from the ideal gas law using a specific gas constant of $\Re$ = 190.7817 J/kg-K corresponding to an atmospheric composition of 96% CO2, 1.93% Ar and 1.89% N2 [46]. The atmosphere reconstruction was performed over an altitude range from approximately 73 km, where there begins to be sufficient signal in the pressure measurements, down to the parachute deployment condition at 10 km. Figure 15(a) shows the the reconstructed densities from the ADB and MEADS reconstructions. A MCS profile taken just prior to landing is included for comparison, along with the pre-flight mean atmosphere model. The uncertainties are shown in Figure 15(b). The reconstructions are generally in good agreement with each other and with the MCS data. The reconstructions indicate the density was higher than the mean pre-flight model at altitudes above 40 km. The higher density was deemed to have been the root cause of the Mars 2020 early guidance start [42] that was observed during EDL. The mean atmosphere is a closer to match to the reconstruction below 40 km.

The reconstructed temperature is shown in Figure 15(c), and uncertainties are shown in Figure 15(d). The ADB reconstruction exhibits more noise than the MEADS reconstruction but in general the two reconstructions are in good agreement for altitudes below 60 km. The ADB-derived temperature uncertainties are high above this range. The ADB-derived temperature also exhibits more noise beginning at the time of the entry ballast mass ejections prior to parachute deployment whereas the MEADS reconstruction remains fairly smooth.

Winds were estimated as filter states throughout EDL althrough observability of winds comes primarily from the off-stagnation supersonic pressure ports. These ports de-saturated in the supersonic flight regime in the altitude range of 14.07 to 10.04 km. The reconstructed winds tracked the nominal winds prior to the supersonic transducer desaturation. After desaturation, the observability of winds was increased and the filter began to adjust its estimate of winds according to the pressure measurements. The results are shown in Figure 16. The reconstructed winds in his altitude range exhibit some transient oscillations that are potentially systematic errors from residual transducer response that are mapped from vehicle motion into the wind estimates. In a mean sense the reconstructed winds are close to the mean winds from the pre-flight model. There is no evidence of any unsual winds, unlike MSL, which saw noticeable cross winds and tail winds during different phases of EDL [5, 7].

The atmosphere conditions estimated from the MEADS pressure data were used in conjunction with other data sources to form a best estimate of the as-flown atmosphere profile from entry interface to landing. The MEADS reconstruction was combined with MCS profiles, global climate modeling data, and with surface pressure measurements from the MEDA instrument on the rover. A temperature profile was constructed by combining these data sources over

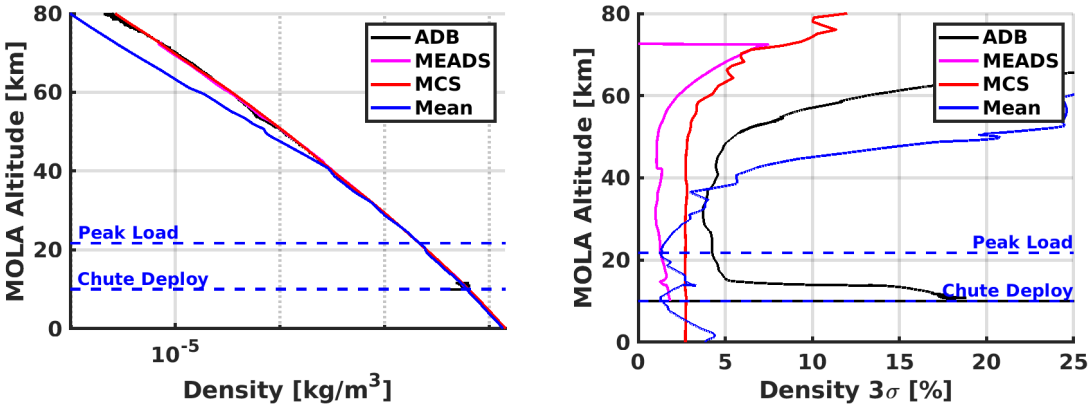


(a) Density

(b) Density Uncertainty

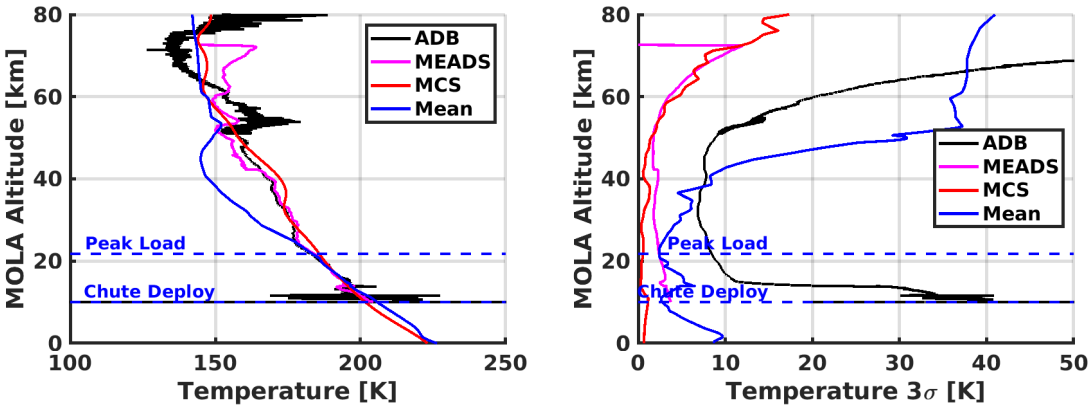


(c) Temperature

(d) Temperature Uncertainty

**Fig. 15 Reconstructed Atmosphere**

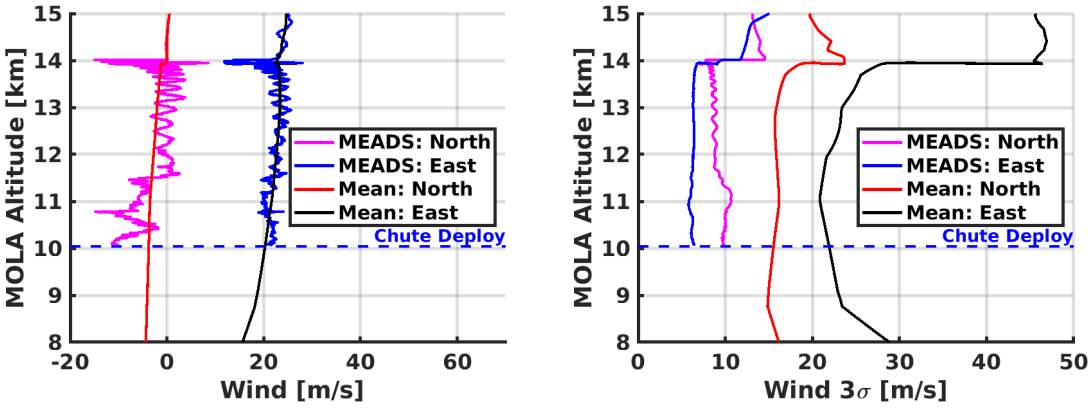


(a) Wind

(b) Wind Uncertainty

**Fig. 16 Reconstructed Winds**

their valid altitude ranges, then the hydrostatic equation was integrated from the surface to the top of the atmosphere along this temperature profile, using the MEDA pressure measurement as the initial condition. Density was then

computed from the ideal gas law. Further details can be found in [47] and comparisons with pre-flight modeling in [48].

### F. Trajectory Events

A summary of the conditions at several events in the trajectory is provided in Tables 8. Event times are given relative to the on-board GN&C initialization time of $t_0$ = 666951979.500504 s. Note that the atmospheric-relative quantities specified here are based on the entry-to-landing reconstructed atmosphere profile described in [47] and may differ slightly from directly reconstructed values reported earlier in this section.

**Table 8 Trajectory Conditions at Events**

| Event | Time from $t_0$ | Mach Number | Dynamic Pressure | Wind-Relative Velocity | MOLA Altitude | Flight Path Angle | Total Angle Of Attack |
|---|---|---|---|---|---|---|---|
| | *sec* | | *Pa* | *m/s* | *km* | *deg* | *deg* |
| Initial Condition | -9.834 | N/A | 0.0 | 4672.85 | 1450.84 | -40.07 | -25.16 |
| GN&C Init | 0.0 | N/A | 0.0 | 4684.25 | 1421.32 | -39.75 | 8.17 |
| Entry Interface | 540.140 | 27.26 | 0.0 | 5333.56 | 128.22 | -16.18 | -16.71 |
| Guidance Start | 591.000 | 27.44 | 506.14 | 5380.99 | 58.86 | -13.31 | -17.44 |
| Mach 25 | 606.503 | 25.00 | 3802.08 | 5168.30 | 40.69 | -12.22 | -15.22 |
| MPH4 Saturation | 607.124 | 24.78 | 4032.24 | 5150.38 | 40.00 | -12.18 | -15.96 |
| Bank Reversal 1 | 621.874 | 20.12 | 12664.32 | 4286.01 | 25.81 | -10.71 | -16.42 |
| Mach 20 | 622.187 | 20.00 | 12858.87 | 4257.58 | 25.56 | -10.66 | -16.46 |
| Peak Load | 627.692 | 17.17 | 14309.32 | 3716.71 | 19.47 | -9.12 | -16.67 |
| Mach 15 | 632.032 | 15.00 | 13767.84 | 3285.44 | 16.10 | -7.82 | -16.53 |
| Bank Reversal 2 | 642.124 | 11.00 | 10444.87 | 2431.93 | 16.09 | -5.24 | -17.02 |
| Mach 10 | 645.272 | 10.00 | 9184.26 | 2222.82 | 15.47 | -4.30 | -17.20 |
| MPH4 Desaturation | 664.249 | 6.35 | 4253.25 | 1413.38 | 14.07 | -0.97 | -18.32 |
| Bank Reversal 3 | 670.124 | 5.68 | 3434.99 | 1263.61 | 13.97 | -0.56 | -18.57 |
| Mach 5 | 677.772 | 5.00 | 2678.28 | 1108.89 | 13.92 | 0.07 | -17.97 |
| EBM Jettison | 763.750 | 2.07 | 571.57 | 466.77 | 11.74 | -9.55 | -22.44 |
| Chute Deploy | 780.750 | 1.82 | 517.76 | 414.38 | 10.04 | -16.26 | -0.39 |
| Heatshield Sep | 803.374 | 0.63 | 76.19 | 145.63 | 7.92 | -31.40 | 14.21 |
| Backshell Sep | 897.671 | 1.82 | 47.63 | 82.14 | -0.34 | -81.30 | -14.50 |
| Touchdown | 958.874 | 0.02 | 0.30 | 6.10 | -2.56 | -76.17 | -83.81 |

## V. Conclusions

The Mars 2020 entry capsule flew a heatshield and backshell that were instrumented with various sensors to make measurements of the aerodynamic and aerothermodynamic environments during entry, descent, and landing on Mars, which occured on February 18th, 2021. The sensors included seven pressure sensors on the heatshield, and one pressure sensor on the backshell. The data acquired from the heatshield pressure sensors was processed in a Kalman filter algorithm to determine the atmospheric-relative trajectory, as-flown atmosphere, and as-flown vehicle aerodynamics. The results indicate the upper altitude atmospheric density was as much as 150% higher than nominal, which is consistent with the observed early entry guidance start time. The density below 40 km was a within 12% of the pre-flight predictions. The reconstructed axial force coefficient was approximately 2% lower than the pre-flight prediction across the entire flight range.

## Acknowledgments

The authors appreciate helpful inputs from Chris Kuhl, Henry Wright, Todd White, Nick Trombetta, and Mike Wilson. The raw DIMU data was provided by Swati Mohan. The TRN data was provided by Andrew Johnson.

## References

[1] Nelessen, A., Sackier, C., Clack, I., Brugarolas, P., Villar, G., Chen, A., Stehura, A., Otero, R., Stilley, E., Way, D., Edquist, K., Mohan, S., Giovingo, C., and Lefland, M., "Mars 2020 Entry, Descent, and Landing System Overview," IEEE Aerospace Conference, March 2019. https://doi.org/10.1109/AERO.2019.8742167

[2] Hwang, M., Bose, D., White, T., Wright, H., Schoenenberger, M., Kuhl, C., Trombetta, D., Santos, J., Oishi, T., Karlgaard, C., Kuhl, C., Mahzari, M., and Pennington, S., "Mars 2020 Entry, Descent and Landing Instrumentation (MEDLI2)," AIAA Paper 2016-3536, AIAA Thermophysics Conference, Washington, DC, June 2016. https://doi.org/10.2514/6.2016-3536

[3] White, T. R., Mahzari, M., Miller, R. A., Tang, C. Y., Monk, J., Santos, J., Karlgaard, C. D., Alpert, H., S., Wright, H. S., and Kuhl, C., "Mars Entry Instrumentation Flight Data and Mars 2020 Entry Environments," AIAA Paper 2022-XXXX, AIAA Sci Tech Forum, San Diego, CA, January 2022.

[4] Cheatwood, F. M., Bose, D., Karlgaard, C. D., Kuhl, C. A., Santos, J. A., Wright, M. J., "Mars Science Laboratory (MSL) Entry, Descent, and Landing Instrumentation (MEDLI): Complete Flight Data Set," NASA TM-2014-218533, October 2014.

[5] Karlgaard, C. D., Kutty, P., Schoenenberger, M., Munk, M. M., Little, A., Kuhl, C. A., and Shidner, J., "Mars Science Laboratory Entry Atmospheric Data System Trajectory and Atmosphere Reconstruction," *Journal of Spacecraft and Rockets*, Vol. 51, No. 4, 2014, pp. 1029–1047. https://doi.org/10.2514/1.A32770

[6] Schoenenberger, M., Van Norman, J., Karlgaard, C. D., Kutty, P., and Way, D., "Assessment of the Reconstructed Aerodynamics of the Mars Science Laboratory Entry Vehicle," *Journal of Spacecraft and Rockets*, Vol. 51, No. 4, 2014, pp. 1076–1093. https://doi.org/10.2514/1.A32794

[7] Chen, A., Cianciolo, A., Vasavada, A., Karlgaard, C., Barnes, J., Cantor, B., Hinson, D., Kass, D., Lewis, S., Mischna, M., Rafkin, S., Tyler, D., "Reconstruction of Atmospheric Properties from the Mars Science Laboratory Entry, Descent, and Landing," *Journal of Spacecraft and Rockets*, Vol. 51, No. 4, 2014, pp. 1062–1075. https://doi.org/10.2514/1.A32708

[8] Edquist, K. T., Hollis, B. R., Johnston, C. O., Bose, D., White, T. R., and Mahzari, M., "Mars Science Laboratory Heat Shield Aerothermodynamics: Design and Reconstruction," *Journal of Spacecraft and Rockets*, Vol. 51, No. 4, 2014, pp. 1106–1124. https://doi.org/10.2514/1.A32749

[9] Bose, D., White, T., Mahzari, M., and Edquist, K., "Reconstruction of Aerothermal Environment and Heat Shield Response of Mars Science Laboratory," *Journal of Spacecraft and Rockets*, Vol. 51, No. 4, 2014, pp. 1174–1184. https://doi.org/10.2514/1.A32783

[10] Dutta, S., Braun, R. D., and Karlgaard, C. D., "Atmospheric Data System Sensor Placement Optimization for Mars Entry, Descent, and Landing," *Journal of Spacecraft and Rockets*, Vol. 51, No. 1, 2014, pp. 163–174. https://doi.org/10.2514/1.A32515

[11] Karlgaard, C. D., Kutty, P. M., and Schoenenberger, M., "Coupled Inertial Navigation and Flush Air Data Sensing Algorithm for Atmosphere Estimation," *Journal of Spacecraft and Rockets*, Vol. 54, No. 1, 2017, pp. 128-140. https://doi.org/10.2514/1.A33331

[12] Schoenenberger, M., Brown, T. G., and Yates, L., "Surface Pressure Ballistic Range Test of Mars 2020 Capsule in Support of MEDLI2," AIAA Paper 2017-4079, June 2017. https://doi.org/10.2514/6.2017-4079

[13] Karlgaard, C. D., Schoenenberger, M., Trombetta, D., and Van Norman, J., "Mars Entry, Descent, and Landing Instrumentation 2 Entry Air Data System Modeling, Calibration, and Performance Analysis," NASA TM, 2021 (to be published).

[14] San Martin, M., Mendeck, G. F., Brugarolas, P. B., Singh, G., Serricchio, F., Lee, S. W., Wong, E. C., and Essmiller, J. C., "In-Flight Experience of the Mars Science Laboratory Guidance, Navigation, and Control system for Entry, Descent, and Landing," *CEAS Space Journal*, Vol. 7, June 2015, pp. 119-142. https://doi.org/10.1007/s12567-015-0091-3

[15] Chen, C. W. and Pollard, B. D., "Radar Terminal Descent Sensor Performance During Mars Science Laboratory Landing," *Journal of Spacecraft and Rockets*, Vol. 51, No. 4, 2014, pp. 1208–1216. https://doi.org/10.2514/1.A32641

[16] Johnson, A., Aaron, S., Chang, J., Cheng, Y., Montgomery, J., Mohan, S., Schroeder, S., Tweddle, B., Trawny, N., and Zheng, J., "The Lander Vision System for Mars 2020 Entry Descent and Landing," AAS Paper 17-036, February 2017.

[17] Mohan, S., Johnson, A. E., Brugarolas, P., Cheng, Y., Otero, R., Trawny, N., Aaron, S., Serricchio, F., Montgomery, J., Casoliva, J., and Chen, A., "Assessment of M2020 Terrain Relative Landing Accuracy: Flight Performance vs. Predicts," AAS Paper 21-541, August 2021.

[18] Seubert, J., Gustafson, E., Jesick, M., Kangas, J., Kruizinga, G., Martin-Mur, T., McCandless, S. E., McElrath, T., Mottinger, N., Ryne, M., Wagner, S., and Wong, M., "Orbit Determination for the Mars 2020 Mission," AAS Paper 21-503, August 2021.

[19] McEwan, A., Eliason, E. M., Bergstrom, J. W., Bridges, N. T., Hansen, C. J., Delamere, W. A., Grant, J. A., Gulick, V. C., Herkenhoff, K. E., Keszthelyi, L., Kirk, R. L., Mellon, M. T., Squyres, S. W., Thomas, N., Weitz, C. M., "Mars Reconnaissance Orbiter's High Resolution Imaging Science Experiment (HiRISE)," *Journal of Geophysical Research*, Vol. 112, No. E5, 2007, Paper E05S02. https://doi.org/10.1029/2005JE002605

[20] Abilleira, F., *at al*, "Mars 2020 Perseverance Trajectory Reconstruction and Performance From Launch Through Landing," AAS Paper 21-518, August 2021.

[21] McCleese, D. J., Schofield, J. T., Taylor, F. W., Calcutt, S. B., Foote, M. C., Kass, D. M., Leovy, C. B., Paige, D. A., Read, P. L., and Zurek, R. W., "Mars Climate Sounder: An Investigation of Thermal and Water Vapor Structure, Dust and Condensate Distributions in the Atmosphere, and Energy Balance of the Polar Regions," *Journal of Geophysical Research*, Vol. 112, No. E5, 2007, Paper E05S06. https://doi.org/10.1029/2006JE002790

[22] Rodriguez-Manfredi, J. A., de la Torre Juarez, M., *et al*, "The Mars Environmental Dynamics Analyzer, MEDA. A Suite of Environmental Sensors for the Mars 2020 Mission," *Space Science Reviews*, Vol 217, No. 48, 2021, pp. 1–86. https://doi.org/10.1007/s11214-021-00816-9

[23] Konopliv, A. S., Asmar, S. W., Folkner, W. M., Karatekin, O., Nunes, D. C., Smrekar, S. E., Yoder, C. F., and Zuber, M. T., "Mars High Resolution Gravity Fields from MRO, Mars Seasonal Gravity, and Other Dynamical Parameters," *Icarus*, Vol. 211, No. 1, 2011, pp. 401–428. https://doi.org/10.1016/j.icarus.2010.10.004

[24] Gorski, K. M., Bills, B. G., and Konopliv, A. S., "A High Resolution Mars Surface Gravity Grid," *Planetary and Space Science*, Vol. 160, October 2018, pp. 84–106. https://doi.org/10.1016/j.pss.2018.03.015

[25] Karlgaard, C. D., Tartabini, P. V., Blanchard, R. C., Kirsch, M., and Toniolo, M. D., "Hyper–X Post–Flight Trajectory Reconstruction," *Journal of Spacecraft and Rockets*, Vol. 43, No. 1, 2006, pp. 105–115. https://doi.org/10.2514/1.12733

[26] Karlgaard, C. D., Beck, R. E., Derry, S. D., Brandon, J. M., Starr, B. R., Tartabini, P. V., and Olds, A. D., "Ares I-X Trajectory Reconstruction: Methodology and Results," *Journal of Spacecraft and Rockets*, Vol. 50, No. 3, 2013, pp. 641–661. https://doi.org/10.2514/1.A32345

[27] Karlgaard, C. D., Kutty, P., O'Farrell, C., Blood, E. M, Ginn, J., and Schoenenberger, M., "Reconstruction of Atmosphere, Trajectory, and Aerodynamics for the Low Density Supersonic Decelerator Test Vehicles," *Journal of Spacecraft and Rockets*, Vol. 56, No. 1, 2019, pp. 221–240. https://doi.org/10.2514/1.A34223

[28] Dutta, S., Karlgaard, C. D., Tynis, J. A., O'Farrell, C. A., Sonneveldt, B. S., Queen, E. M., Bowes, A. L., Leylek, E. A., and Ivanov, M. C., "Advanced Supersonic Parachute Inflation Research Experiment Preflight Trajectory Modeling and Postflight Reconstruction," *Journal of Spacecraft and Rockets*, Vol. 57, No. 6, 2020, pp. 1387–1407. https://doi.org/10.2514/1.A34706

[29] Alpert, H., Mahzari, M., Saunders, D., Monk, J., and White, T. R., "Inverse Estimation of Mars2020 Entry Aeroheating Environments Using MEDLI2 Flight Data," AIAA Paper 2021-XXXX, AIAA Sci Tech Forum, San Diego, CA, January 2022.

[30] Miller, R. A., Tang, C. Y., White, T. R., and Cruden, B. A., "MEDLI2: MISP Measured Aftbody Aerothermal Environments," AIAA Paper 2021-XXXX, AIAA Sci Tech Forum, San Diego, CA, January 2022.

[31] Tang, C. Y., Mahzari, M., Prabhu, D. K., Alpert, H., Cruden, B. A., "MEDLI2: MISP Inferred Aerothermal Environment and Flow Transition Assessment," AIAA Paper 2021-XXXX, AIAA Sci Tech Forum, San Diego, CA, January 2022.

[32] Edquist, K. T., Johnston, C. O., Wise, A. J., and Mahzari, M., "Mars 2020 Reconstructed Aerothermal Environments and Thermal Protection System Assessment," AIAA Paper 2021-XXXX, AIAA Sci Tech Forum, San Diego, CA, January 2022.

[33] Tapley, B. D., Schutz, , B. E., and Born, G. H., *Statistical Orbit Determination*, Elsevier, 2004, Chapter 2, Chapter 6.

[34] Seidelmann, P. K., Abalakin, V. K., Bursa, M., Davies, M. E., de Burgh, C., Lieske, J. H., Oberst, J., Simon, J. L., Standish, E. M., Stooke, P., and Thomas, P. C., "Report of the IAU/IAG Working Group on Cartographic Coordinates and Rotational Elements of the Planets and Satellites: 2000," *Celestial Mechanics and Dynamical Astronomy*, Vol. 82, 2002, pp. 83–111. https://doi.org/10.1023/A:1013939327465

[35] Serricchio, F., San Martin, A. M., Brugarolas, P., and Casoliva, J., "The Mars 2020 Perseverance Navigation Filter," AAS Paper 21-539, August 2021.

[36] Winder, S., *Analog and Digital Filter Design, Second Edition*, Elsevier Science, 2002, Chapter 2.

[37] Oppenheim, A. V. and Schafer, R. W., *Discrete-Time Signal Processing*, Pearson, 3rd edition, 2010, Chapter 5.

[38] Karlgaard, C. D., Korzun, A. M., Schoenenberger, M., Bonfiglio, E. P., Kass, D. M., and Grover, M. R., "Mars InSight Entry, Descent, and Landing Trajectory and Atmosphere Reconstruction," *Journal of Spacecraft and Rockets*, Vol. 58, No. 3, 2021, pp. 865–878. https://doi.org/10.2514/1.A34913

[39] Fergason, R. L., Hare, T. M., Kirk, R. L., Piqueux, S., Galuzska, D. M., Golombek, M. P., Otero, R. E., and Redding, B. L., "Mars 2020 Landing Site Evaluation: Slope and Physical Property Assessment," 48th Lunar and Planetary Science Conference, 20-24 March 2017, The Woodlands, Texas. LPI Contribution No. 1964, id.2163.

[40] Pong, C. M., Collins, S. M., Mohan, S., Serricchio, F., Brugarolas, P., San Martin, A. M., and Lo, K. D., "Analysis of the Mars 2020 Perseverance Entry, Descent, and Landing Attitude Initialization Performance," AAS Paper 21-563, August 2021.

[41] Smith, D. E., Zuber, M. T., Frey, H. V., Garvin, J. B., Head, J. W., Muhleman, D. O., Pettengill, G. H., Phillips, R. J., Solomon, S. C., Zwally, H. J., Banerdt, W. B., Duxbury, T. C., Golombek, M. P., Lemoine, F. G., Neumann, G. A., Rowlands, D. D., Aharonson, O., Ford, P. G., Ivanov, A. B., Johnson, C. L., McGovern, P. J., Abshire, J. B., Afzal, R. S., and Sun, X., "Mars Orbiter Laser Altimeter: Experiment Summary After the First Year of Global Mapping of Mars," *Journal of Geophysical Research*, Vol. 106, No. E10, pp. 23,689–23,722, 2001. https://doi.org/10.1029/2000JE001364

[42] Way, D. W., Dutta, S., Zumwalt, C., and Blette, D., "Assessment of the Mars 2020 Entry, Descent, and Landing Simulation," AIAA Paper 2022-XXXX, AIAA Sci Tech Forum, San Diego, CA, January 2022.

[43] Kutty, P., "Reconstruction and Uncertainty Quantification of Entry, Descent, and Landing Trajectories Using Vehicle Aerodynamics," M. S. Thesis, School of Aerospace Engineering, Georgia Institute of Technology, May 2014.

[44] Schoenenberger, M., Kutty, P., Queen, E., and Karlgaard, C., "The Aerodynamics of Axisymmetric Blunt Bodies Flying at Angle of Attack," IEEE Aerospace Conference, Big Sky, MT, March 2014. https://doi.org/10.1109/AERO.2014.6836312

[45] Schoenenberger, M., Karlgaard, C., Dutta, S., and Van Norman, J., "Assessment of the Reconstructed Aerodynamics of the Mars 2020 Entry Vehicle," AIAA Aviation Forum, Chicago, IL, June 2022. (to be published)

[46] Mahaffy, P. R., Webster, C. R., Atreya, S. K., Franz, H., Wong, M., Conrad, P. G., Harpold, D., Jones, J. J., Leshin, L. A., Manning, H., Owen, T., Pepin, R. O., Squyres, S., and Trainer, M., "Abundance and Isotopic Composition of Gases in the Martian Atmosphere from the Curiosity Rover," *Science*, Vol. 341, July 2013, pp. 263-266. https://doi.org/10.1126/science.1237966

[47] Dutta, S., Karlgaard, C. D., Kass, D., Villar, G., and Mischna, M., "Post-flight Analysis of Atmospheric Properties from Mars 2020 Entry, Descent, and Landing," AIAA Paper 2022-XXXX, AIAA Sci Tech Forum, San Diego, CA, January 2022.

[48] Mischna, M., Villar, G., Kass, D., Dutta, S., Rafkin, S., Tyler, D., Barnes, J., Cantor, B., Lewis, S., Hinson, D., Pla-Garcia, J., Kleinbohl, A., and Karlgaard, C., "Pre- and Post-Entry, Descent and Landing Assessment of the Martian Atmosphere for the Mars 2020 Rover," *The Planetary Science Journal*, (to be published).